polymers

MDPI

Article

Copper Nanoparticles Decorated Alginate/Cobalt-Doped Cerium Oxide Composite Beads for Catalytic Reduction and Photodegradation of Organic Dyes

Hamed A. Alshaikhi [1], Abdullah M. Asiri [1,2], Khalid A. Alamry [1], Hadi M. Marwani [1,2], Soliman Y. Alfifi [1] and Sher Bahadar Khan [1,2,*]

[1] Chemistry Department, Faculty of Science, King Abdulaziz University, P.O. Box 80203, Jeddah 21589, Saudi Arabia
[2] Center of Excellence for Advanced Materials Research, King Abdulaziz University, P.O. Box 80203, Jeddah 21589, Saudi Arabia
* Correspondence: sbkhan@kau.edu.sa

Abstract: Cobalt-doped cerium oxide (Co–CeO_2) was synthesized and wrapped inside alginate (Alg) hydrogel beads (Alg/Co–CeO_2). Further, copper nanoparticles (Cu) were grown on Alg/Co–CeO_2 beads. Cu decorated Alg/Co–CeO_2 composite beads (Cu@Alg/Co–CeO_2) were tested as a catalyst for the solar-assisted photodegradation and $NaBH_4$-assisted reduction of organic pollutants. Among different dyes, Cu@Alg/Co–CeO_2 was found to be the best catalyst for the photodegradation of acridine orange (ArO) under solar light and efficient in reducing methyl orange (MO) with the aid of $NaBH_4$. Cu@Alg/Co–CeO_2 decolorized ArO up to 75% in 5 h under solar light, while 97% of MO was reduced in 11 min. The decolorization efficiency of Cu@Alg/Co–CeO_2 was further optimized by varying different parameters. Thus, the designed catalyst provides a promising way for efficient oxidation and reduction of pollutants from industrial effluents.

Keywords: copper nanoparticles; alginate; Co–CeO_2; nanocatalyst; photodegradation; reduction; dyes; organic pollutants; water treatment

Citation: Alshaikhi, H.A.; Asiri, A.M.; Alamry, K.A.; Marwani, H.M.; Alfifi, S.Y.; Khan, S.B. Copper Nanoparticles Decorated Alginate/Cobalt-Doped Cerium Oxide Composite Beads for Catalytic Reduction and Photodegradation of Organic Dyes. *Polymers* **2022**, *14*, 4458. https://doi.org/10.3390/polym14204458

Academic Editors: Wei Guo and Mu Naushad

Received: 19 June 2022
Accepted: 19 September 2022
Published: 21 October 2022

1. Introduction

Advances in the food automation, textile, paper, and leather industries have promoted the usage of organic dyes. These industries and tanneries are the main sources of organic pollutants, and their physical presence in wastewater has given the earth an unpleasant look, becoming a global concern [1–3]. The presence of these dyes' pollutants at very low concentrations in wastewater cannot be removed by sedimentation and ordinary chemical degradation since dyes are very stable, carcinogenic, and mutagenic in nature for humans and living organisms [4,5]. Therefore, it is important to remove these effluents from discharged wastewater. Several methods have been used for their removal, such as biodegradation [6–8], thermal radiation [9], fenton [10,11], chemical reduction [12], microbial catabolism [13,14], ultrasonic excitement [15], and photocatalytic degradation [16–18]. Some of these methods cannot completely remove these effluents. Therefore, a green procedure, i.e., photocatalytic degradation and catalytic reduction, is needed to eliminate these hazardous pollutants. These methods require an efficient catalyst and sunlight/strong reducing agent to catalyze the degradation/reduction [16–19].

Metal oxides (MOs) and zero-valent metal nanoparticles (MNPs) have attracted significant attention because MOs have shown significant properties and have been used in different applications [16–21]. Therefore, fabricating a suitable catalyst possessing appreciable activity with fast electron donor and acceptor ability is highly required. Doped MOs and MNPs, i.e., Cu, Ag, Ni, Co, etc., have played a vital role in photocatalysis and catalytic reduction of organic pollutants [21–23]. However, these NPs are prone to aggregation due

to their high surface energy, which limits their catalytic property [24]. Additionally, they cannot be easily separated from aqueous solution for reuse. Hence, various supportive surfaces have been employed to stabilize these MNPs [25–29].

Polymer composites and hydrogels combined with nanoparticles, which reinforce the mechanical properties of hydrogels, manifest more efficiently. They exhibit stimuli-responsive characteristics, including catalysis, drug degradation, elimination of aquatic pollution, and other features, which are reasons to consider them "smart" materials [30–33]. Concerning wastewater processing, hydrogel-based composites exhibit top efficacy in the reduction of various species for different contaminants [34]. Hydrogels being highly hydrophilic provides quasi-homogeneous traits to nanoparticles, hence improving their catalytic activity [35]. For more than a decade, a wide range of research has been carried out to improve incoming photocatalytic nanohybrids as emerging materials for wastewater remediation. A synthetic route may affect the catalytic performance of hybrid materials [36]. Metal-based nanomaterials have been given significant attention in different applications, especially their high efficiency in catalysis [37–41]. In a previous study, a metal oxide nanocatalyst was found to be highly selective, as it showed greater effectiveness in reducing potassium hexacyanoferrate ($K_3[Fe(CN)_6]$) [42]. Currently, new treatment technologies for dyes are needed, which can clear dyes from wastewater and minimize the exposure of toxic chemicals to humans and the environmental system [43]. Photocatalytic degradation and catalytic reduction are the most studied methods for dye removal and conversion of dyes into less toxic products [44].

Doped metal oxides have become one of the most effective materials used as catalysts, especially in nanosized materials. Such materials have shown exceptional characteristics in several applications, especially in reducing and degrading water pollutants. Doping by metals participates in regulating the electronic and catalytic properties of the catalyst and elevating surface area, thus enhancing its catalytic characteristics [35,42].

In this study, Co–CeO_2 was simply prepared and then entrapped inside alginate hydrogel beads. Alg/Co–CeO_2 beads were further dipped in copper solution, where the beads adsorbed Cu from the solution and were converted into Cu nanoparticles by treatment with $NaBH_4$. Cu@Alg/Co–CeO_2 was evaluated as a catalyst for the solar-assisted photodegradation and $NaBH_4$-assisted reduction of organic pollutants. Cu@Alg/Co–CeO_2 was found to be the best catalyst for the photodegradation of acridine orange (ArO) under solar light, as well as a competent catalyst for reducing MO with the aid of $NaBH_4$.

2. Experimental Section

2.1. Chemicals and Reagents

Sodium alginate, cerium nitrate, cobalt nitrate, copper nitrate, 4-nitrophenol (4-NP), 2,6-dinitrophenol (2,6-DNP), sodium hydroxide, 2-nitrophenol (2-NP), acridine orange (ArO), methyl orange (MO), congo red (CR), methylene blue (MB), aluminum chloride, sodium borohydride, and all other utilized chemicals and solvents were purchased from Sigma Aldrich and BDH. Distilled water was utilized in all experiments.

2.2. Synthesis of Co–CeO_2 Nanoparticles

To prepare the Co–CeO_2 nanocomposite, 0.1 molar solution was prepared by dissolving 4.36 g of cerium nitrate and 5.83 g of cobalt nitrate in 100 mL of deionized water. NaOH was then added to increase the pH of the salt solution and then kept on heating (60 °C) with stirring. After 12 h, the precipitate was washed several times with distilled water, dried in an oven at 50 °C, and then calcined at 500 °C [45–48].

2.3. Preparation of Cu@Alg/Co–CeO_2

To prepare Cu@Alg/Co–CeO_2, Co–CeO_2 was ground until it became powder, and then 2.0338 g of Co–CeO_2 powder was taken and dispersed in 30 mL of Alg solution. The solution was mixed together by stirring. The mixture of Co–CeO_2 with Alg was taken in a syringe and added dropwise from the mixture of Alg/Co–CeO_2 to $AlCl_3$ solution. Thus, a

granular form of Alg/Co–CeO_2 was obtained and left in the solution ($AlCl_3$) for a while. Then, the granules were washed with distilled water and completely dried. Alg/Co–CeO_2 granules were placed in the copper solution overnight. Alg/Co–CeO_2 beads entrapped Cu ions and then treated with $NaBH_4$ solution and converted into nanoparticles [49,50].

2.4. Apparatus

For morphology characterization of CeO_2–Co_2O_3 and Cu@Alg/Co–CeO_2, a scanning electron microscope was used, while for compositional analysis, an energy-dispersive spectrometer (EDS) was utilized. The morphology and particle size of the samples were studied using a scanning electron microscope (SEM: JSM-5910, JEOL). For this purpose, a small amount of the powder samples was stuck on aluminum stubs with the help of carbon conducting tape. The stubs were placed in an autofine coater (JFC-1600, JEOL) for sputtering with a thin layer of gold for 30 s. The stubs containing the samples were then placed in the sample chamber of the SEM. After evacuating the machine according to the standard procedures, the samples were investigated for their morphology. The distance of the sample from the tip of the electron gun and the accelerating voltage were adjusted to 10 mm and 15 kV, respectively. The same samples were used for EDX analysis. Removal of organic pollutants was observed by a UV–vis spectrophotometer (Thermo Scientific Evolution 300 UV–visible spectrophotometer, Waltham, MA, USA), which recorded the catalytic experiments at wavelengths between 200 and 800 nm.

2.5. Catalytic Reduction

Cu@Alg/Co–CeO_2 was applied for the reduction of organic pollutants using $NaBH_4$ as a reducing agent, and we evaluated its catalytic activity. Initially, 2.5 mL of pollutants (4-NP (0.13 mM), ArO (0.07 mM), CR (0.07 mM), MO (0.07 mM), MB (0.07 mM), 2,6-DNP (0.13 mM), 2-NP (0.13 mM), and $K_3[Fe(CN)_6]$ (0.5 mM)) was mixed with 0.5 mL of $NaBH_4$ (0.1 M) in a UV cuvette. The different amount (2–10 beads) of Cu@Alg/Co–CeO_2 was introduced to the mixture, and the UV–vis spectrum was taken at different times. The effect of different parameters such as catalyst amount, reducing agent amount, and reusability was checked to optimize the method toward reduction of the most selective dye based on the study. The effectiveness of Cu@Alg/Co–CeO_2 was assessed by Equation (1) [42]:

$$\% \text{ Reduction/Degradation} = \frac{C_o - C_t}{C_o} \times 100 \quad (1)$$

where C_o is the initial concentration/absorbance, and C_t is the concentration/absorbance at time (t) of each individual pollutant.

2.6. Photocatalytic Degradation

Cu@Alg/Co–CeO_2 was also tested as a photocatalyst for the degradation of MO, ArO, CR, and MB. Initially, 10 mL of each pollutant (MO (0.07 mM), ArO (0.07 mM), CR (0.07 mM) and MB (0.07 mM)) was taken in a beaker individually. Then, Cu@Alg/Co–CeO_2 (4–10 beads) was mixed with the pollutant solution and kept under solar light. An amount of 3 mL of solution was taken from the reaction beaker at different times and then recording the UV–vis spectrum. The influence of different parameters such as photocatalyst amount, light source, and reusability was also investigated toward degradation of the most selective dye based on the study. The effectiveness of Cu@Alg/Co–CeO_2 was assessed by Equation (1).

3. Results and Discussion

3.1. Characterization of Co–CeO_2, Alg/Co–CeO_2, and Cu@Alg/Co–CeO_2

First, Co–CeO_2 was prepared and then dispersed in Alg solution. The mixed solution was crosslinked by $AlCl_3$ and produced Alg/Co–CeO_2 beads. Alg/Co–CeO_2 beads were dipped in Cu salt solution, where Cu ions bonded with the COO–, OH, and O groups of Alg/Co–CeO_2. The adsorbed Cu ions were converted into Cu nanoparticles by $NaBH_4$,

and thus Cu nanoparticles were grown inside and on the Alg/Co–CeO_2 beads' surface. The growth of Cu nanoparticles is shown in Scheme 1, and the reduction of Cu nanoparticles by $NaBH_4$ is presented as follows:

$$2Cu^{2+} + 4BH_4^- + 12H_2O \Rightarrow 2Cu^0 + 4B(OH)_3 + 14H_2$$

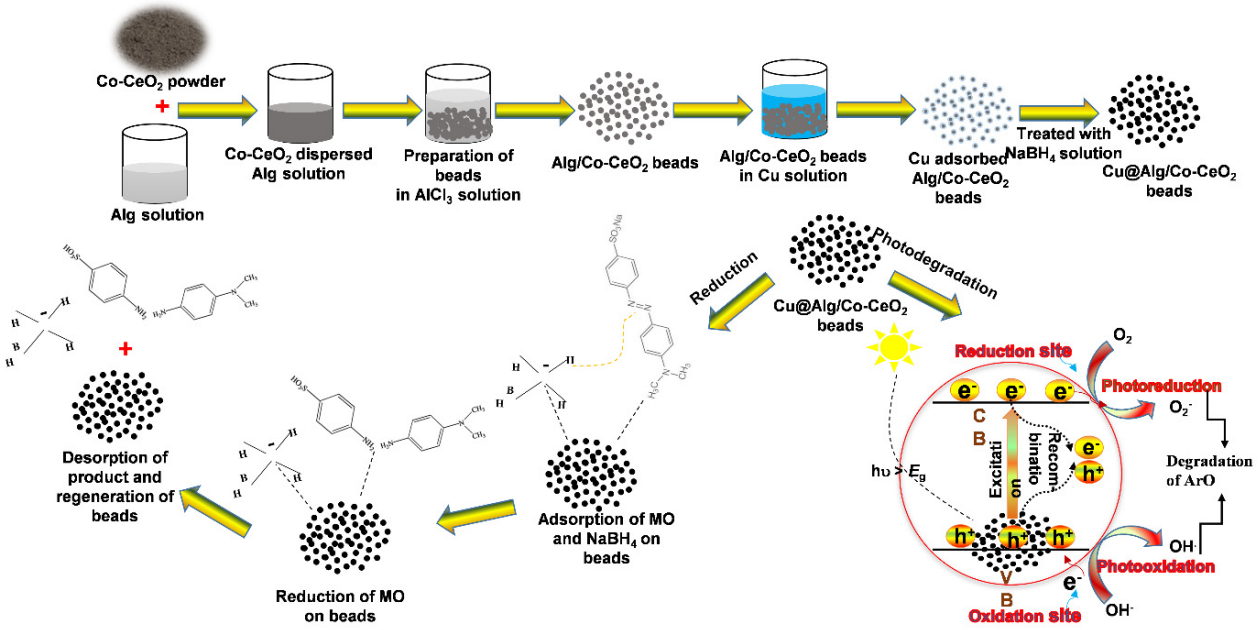

Scheme 1. Schematic representation of preparation and catalytic properties of Cu@Alg/Co–CeO_2.

The morphology of Co–CeO_2, Alg/Co–CeO_2, and Cu@Alg/Co–CeO_2 was assessed from SEM images. SEM images of Co–CeO_2, Alg/Co–CeO_2, and Cu@Alg/Co–CeO_2 are illustrated in Figure 1, where it can be clearly noticed that Co–CeO_2 is grown in high quantities in the form of nanoparticles. Some parts of the picture show the accumulation and aggregation of nanoparticles in the case of Co–CeO_2 (Figure 1a,a'). Alg/Co–CeO_2 shows a loose-fitting rough and irregular surface. Alg/Co–CeO_2 images show a rough surface with pores and grooves (Figure 1b,b'). Alg/Co–CeO_2 images show well-dispersed particles in the hydrogel beads' matrix. This suggests that the hydrogel beads have well-dispersed Co–CeO_2 encapsulated inside. However, Cu@Alg/Co–CeO_2 has a more compact morphology (Figure 1c,c'), along with well-dispersed particles in the hydrogel beads' matrix. These particles reflect the presence of Cu nanoparticles along with well-dispersed Co–CeO_2 inside the hydrogel beads. The morphology of Cu@Alg/Co–CeO_2 changed to a more compact surface containing wrinkles after the growth of Cu nanoparticles on the surface. This indicates that copper ion adsorption, and further its conversion to Cu nanoparticles, causes shrinkage of the polymeric matrix and provides a more compact structure [51]. The growth of Cu nanoparticles causes a change in the surface morphology of Alg/Co–CeO_2 hydrogels.

EDS was utilized to assure the elemental composition of Co–CeO_2, Alg/Co–CeO_2, and Cu@Alg/Co–CeO_2. The spectrum of Co–CeO_2 exhibited Co (36.1 mass %), Ce (36.05 mass %), and O (22.47 mass %) peaks (Figure 2a), while the Alg/Co–CeO_2 spectrum displayed Co, Ce, and O peaks along with C and O elements. Thus, the observed spectrum of Co–CeO_2 confirms that Co–CeO_2 composed of Co, Ce, and O elements, while Alg/Co–CeO_2 contains both Co–CeO_2 and Alg. C and O peaks reflect Alg, which is the major component of Alg/Co–CeO_2 because the mass % of C and O is 22.32 and 57.80, while Co and Ce have a mass % of 8.80 and 11.51 (Figure 2b). EDS of Cu@Alg/Co–CeO_2 exhibited peaks for C, O, Ce, Co, and Cu. C and O peaks represented Alg, Ce and Co due to Co–CeO_2, while Cu appeared due to the presence of Cu nanoparticles (Figure 2c). The mass % obtained for C, O, Ce, Co, and Cu was 22.16, 55.49, 8.80, 11.89, and 1.56, respectively. EDS spectra also

suggest that Co–CeO_2, Alg/Co–CeO_2, and Cu@Alg/Co–CeO_2 are pure because only Co, Ce, and O were observed in Co–CeO_2, C, O, Co, and Ce in the case of Alg/Co–CeO_2 and C, O, Co, Ce, and Cu in the case of Cu@Alg/Co–CeO_2.

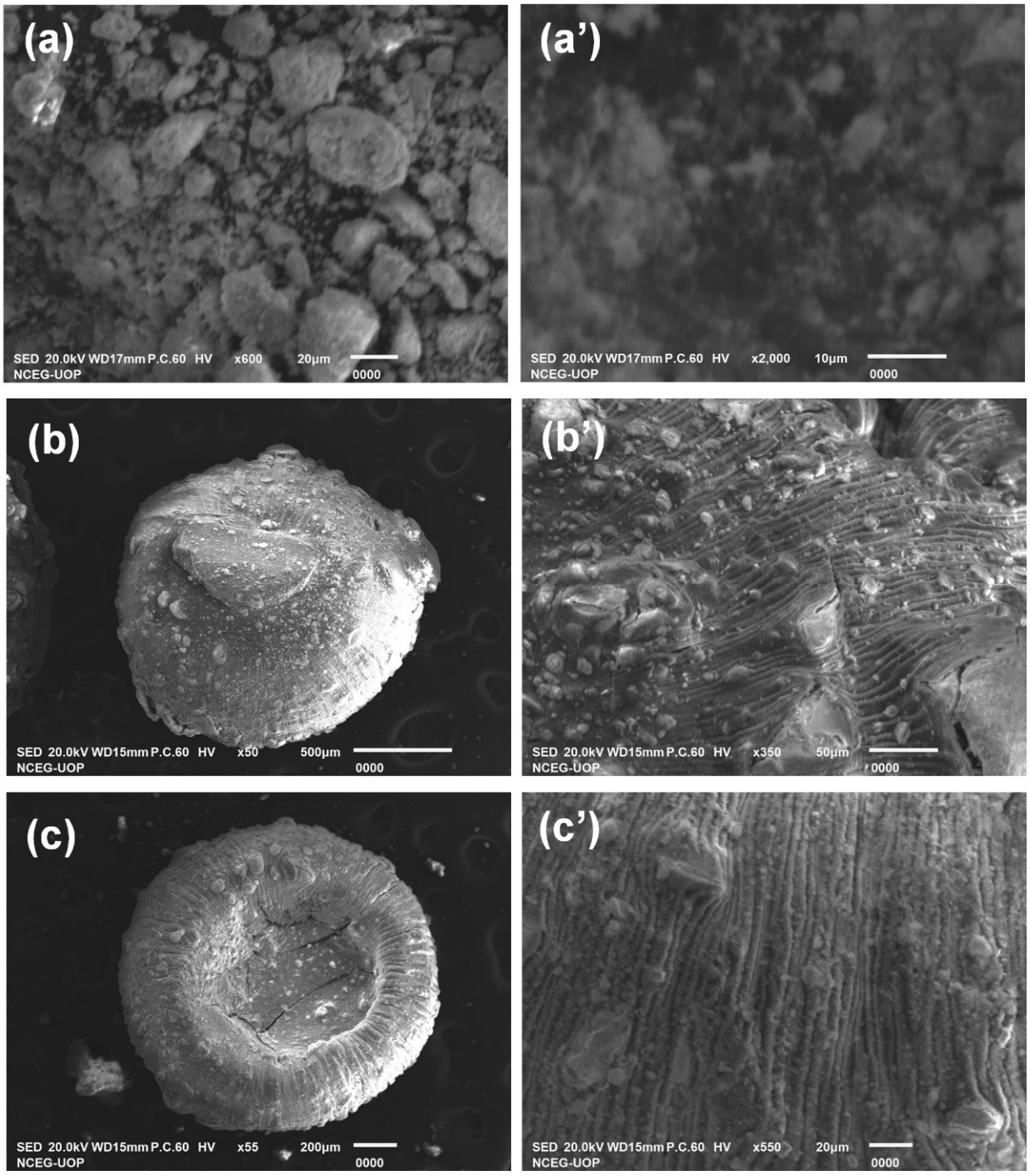

Figure 1. SEM images of (**a**,**a′**) Co–CeO_2, (**b**,**b′**) Alg/Co–CeO_2, and (**c**,**c′**) Cu@Alg/Co–CeO_2.

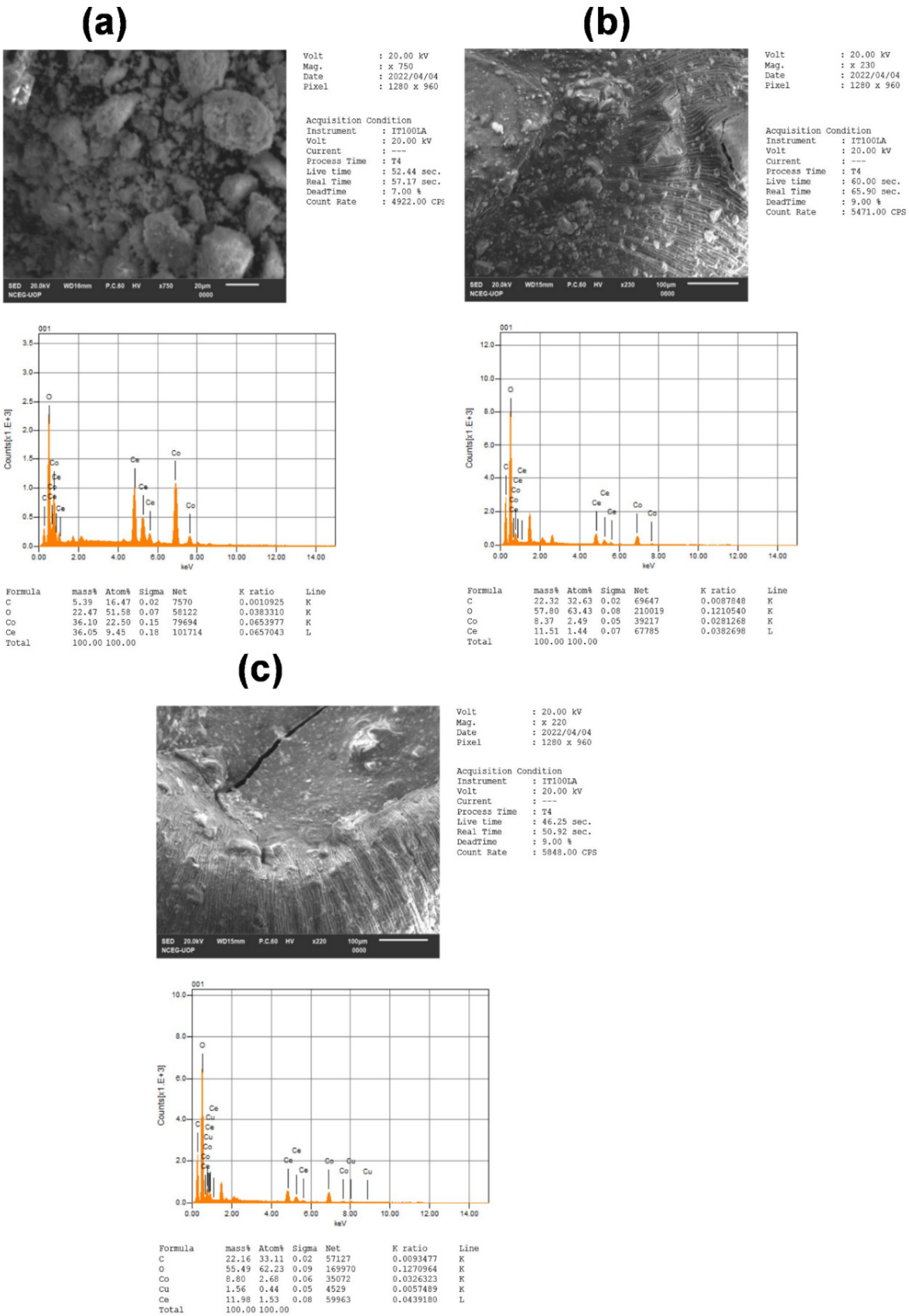

Figure 2. EDS spectra of (**a**) Co–CeO_2, (**b**) Alg/Co–CeO_2, and (**c**) Cu@Alg/Co–CeO_2.

3.2. Water Purification Applications

Recently, several metal oxides have been utilized as catalysts for the removal of toxic pollutants owing to their superior catalytic activity during oxidation or reduction. Such processes are initiated by solar/UV light or strong reducing agents such as $NaBH_4$ using metal oxide nanoparticles as catalysts. In the literature, different pollutants have been catalytically degraded/reduced by employing diverse metallic oxides with the aid of light or $NaBH_4$ [52–54]. Therefore, Cu@Alg/Co–CeO_2 was tested for the catalytic removal of dyes and other contaminants.

3.2.1. Catalytic Reduction

Cu@Alg/Co–CeO_2 demonstrated superior catalytic performance in the presence of $NaBH_4$. Pure Co–CeO_2 exhibited good activity, but the leaching and reusability of Co–CeO_2 in powder form is a challenging task. As it is extremely difficult to separate Co–CeO_2 in nanosized powder form from the reaction mixture for reuse, as well as leaching via filtration, Co–CeO_2 was embedded inside the Alg beads to control the leaching of Co–CeO_2 and increase the possibility of reusability. The catalyst in bead form can easily be pulled from the reaction mixture, washed, and reused in another catalytic reaction. Co–CeO_2 was wrapped inside Alg beads by dispersing it first in Alg solution and then crosslinking it with $AlCl_3$. The beads were further subjected to the growth of Cu nanoparticles, and the developed Cu@Alg/Co–CeO_2 catalyst was tested in reducing different organic pollutants such as dyes, $K_3[Fe(CN)_6]$ and nitrophenols with the aid of $NaBH_4$. Different pollutants such as 4-NP, ArO, CR, MO, MB, 2,6-DNP, 2-NP, and $K_3[Fe(CN)_6]$ were chosen for the current study, where Cu@Alg/Co–CeO_2 was used as a catalyst with the aid of $NaBH_4$ to evaluate its catalytic activity and efficacy as a nanocatalyst. Cu@Alg/Co–CeO_2 was added to each individual pollutant along with $NaBH_4$.

The study steps were as follows: Initially, a 2.5 mL (4-NP (0.13 mM), ArO (0.07 mM), CR (0.07 mM), MO (0.07 mM), MB (0.07 mM), 2,6-DNP (0.13 mM), 2-NP (0.13 mM), and $K_3[Fe(CN)_6]$ (0.5 mM)) of each individual pollutant was taken, and UV–vis absorption was measured for the pure pollutant. After that, 0.5 mL of the $NaBH_4$ (concentration, 0.1 mM) reducing agent was mixed with the pollutant, and UV–vis absorption was measured for each pollutant with the aid of the reducing agent $NaBH_4$; then, four beads of Cu@Alg/Co–CeO_2 were introduced to the mixture, and the UV–vis spectrum of the mixture was taken every minute until the pollutant was completely reduced. Figure 3 displays that the absorbance band of the pollutants decreased steadily when completing the reduction reaction. These findings support that the pollutants were reduced, forming less toxic products by transmitting the electron donor BH_4^- to the catalyst and moving electrons to the acceptor pollutant molecules.

The % reduction was calculated based on Equation (1), and the reduction rates of 4-NP (0.13 mM), ArO (0.07 mM), CR (0.07 mM), MO (0.07 mM), MB (0.07 mM), 2,6-DNP (0.13 mM), 2-NP (0.13 mM), and $K_3[Fe(CN)_6]$ (0.5 mM) with the aid of $NaBH_4$ were calculated based on Equation (2):

$$\ln C_t/C_o = \ln A_t/A_o = -K\mathrm{t} \quad (2)$$

where C_t and C_o are pollutant concentrations, in which A_t (absorbance at a specific time) and A_o (initial absorbance) are equal to C_t and C_o, respectively. k_{app} can be acquired from plotting $\ln(C_t/C_o)$ vs. reduction time (t). $\ln(A_t/A_0)$ vs. time (t) and kinetics of MO reduction by Cu@Alg/Co–CeO_2 are plotted in Figure 4.

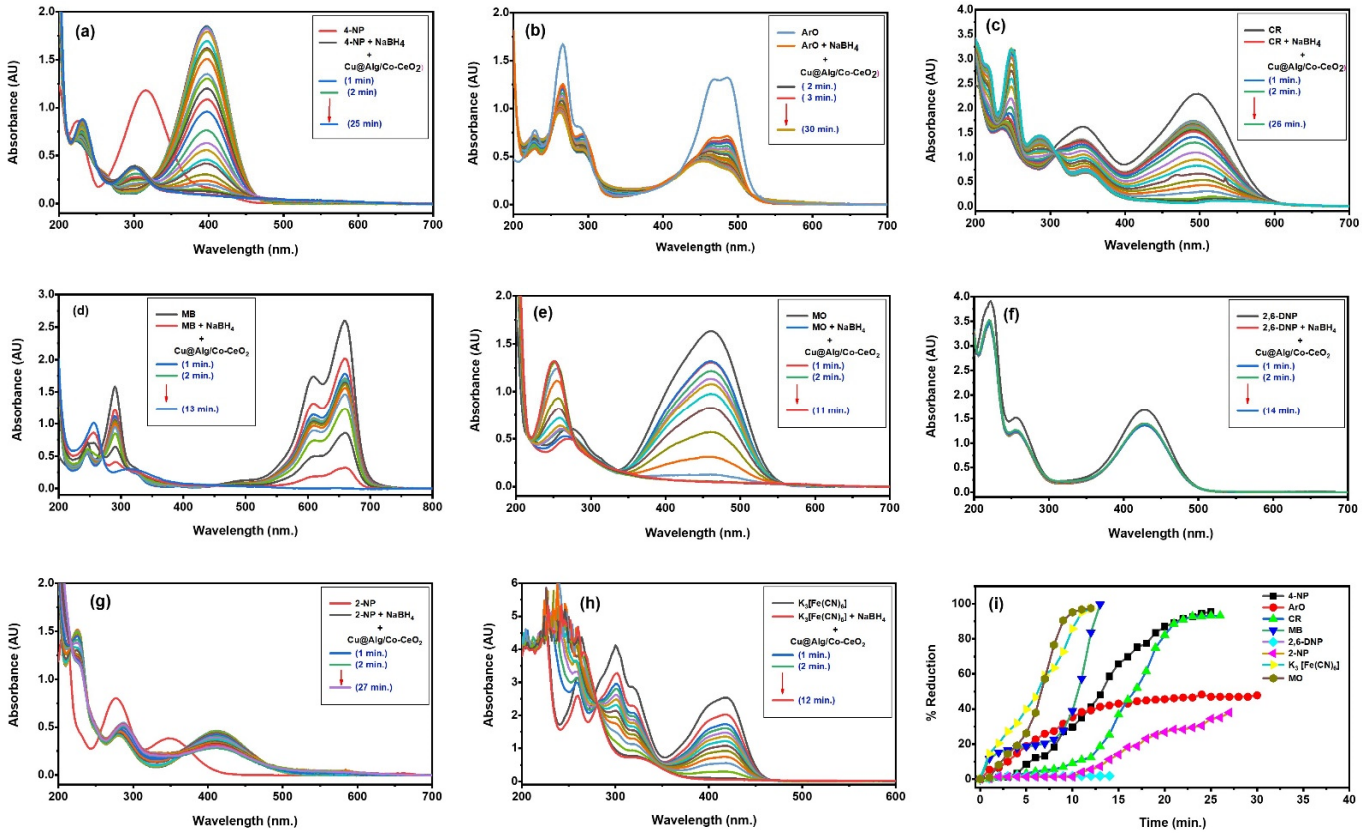

Figure 3. UV–vis absorption spectra for the reduction of pollutants: (**a**) 4-NP (0.13 mM), (**b**) ArO (0.07 mM), (**c**) CR (0.07 mM), (**d**) MO (0.07 mM), (**e**) MB (0.07 mM), (**f**) 2,6-DNP (0.13 mM), (**g**) 2-NP (0.13 mM), and (**h**) $K_3[Fe(CN)_6]$ (0.5 mM)] using 0.5 mL $NaBH_4$ (0.1 M) and Cu@Alg/Co–CeO_2 catalyst (4 beads). (**i**) % Reduction of pollutants as a function of time.

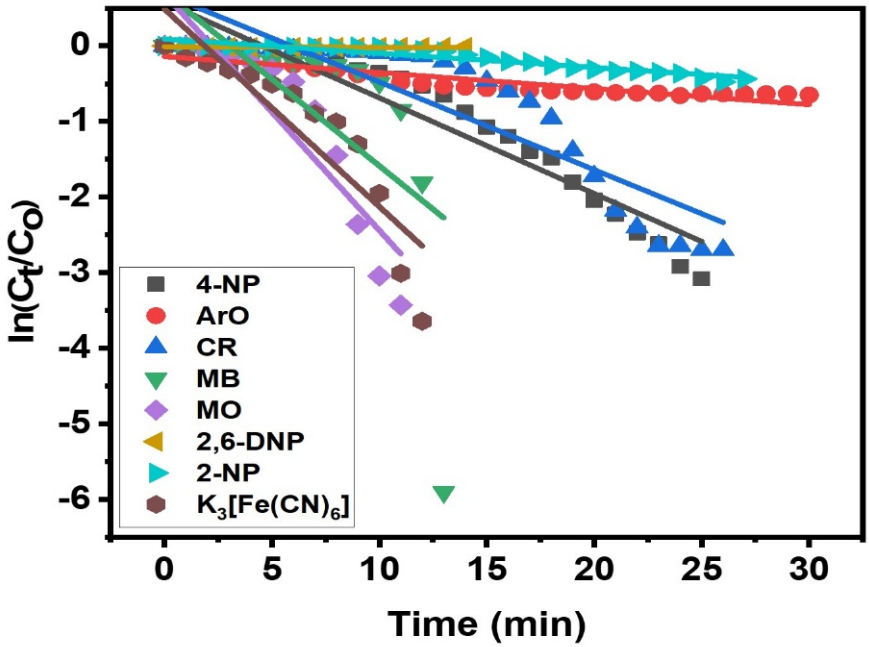

Figure 4. Kinetic study for reduction of 4-NP (0.13 mM), ArO (0.07 mM), CR (0.07 mM), MO (0.07 mM), MB (0.07 mM), 2,6-DNP (0.13 mM), 2-NP (0.13 mM), and $K_3[Fe(CN)_6]$ (0.5 mM) using 0.5 mL $NaBH_4$ (0.1 M) and Cu@Alg/Co–CeO_2 catalyst (4 beads).

The % reduction of the selected pollutants using Cu@Alg/Co–CeO_2 catalyst was found to be high (>95%) for 4-NP, CR, MB, MO, and $K_3[Fe(CN)_6]$ and low (<40%) for ArO, 2,6-DNP, and 2-NP. Table 1 clearly displays % reduction, consumed time, and rate constant for the reduction of each compound. It is clear that MO was reduced in the shortest time compared with the other studied pollutants, providing the highest rate constant equal to 0.3129 min^{-1} using the Cu@Alg/Co–CeO_2 catalyst.

Table 1. Characteristics of catalytic reduction of studied pollutants using $NaBH_4$ and four beads of Cu@Alg/Co–CeO_2.

Pollutant	% Reduction	Time (min)	Rate Constant (min^{-1})
4-NP	95.41	25	0.1267
ArO	47.76	30	0.0212
CR	93.27	26	0.1163
MB	99.73	13	0.2296
MO	97.51	11	0.3129
2,6-DNP	1.71	14	0.0008
2-NP	37.94	27	0.0188
$K_3[Fe(CN)_6]$	97.38	12	0.2615

Cu@Alg/Co–CeO_2 demonstrated superior catalytic activity toward MO in the presence of $NaBH_4$. Thus, Cu@Alg/Co–CeO_2 was more effective for MO reduction. So, MO was selected for detailed investigation, where the optimization of catalyst amount, $NaBH_4$ concentration, and recyclability was performed.

MO reduction by $NaBH_4$ was conducted by employing Cu@Alg/Co–CeO_2 beads as a catalyst. First, Cu@Alg/Co–CeO_2 was introduced into the MO solution along with $NaBH_4$. A decrease in MO absorbance peaks at 460 nm and 270 nm was noticed until the termination of the reaction, with a new peak appearing at 247 nm. Such findings reveal that the azo group (–N=N–) in MO was reduced, producing new products by the transmitting electron donor BH_4^- to the nanocatalyst beads, thus handing over electrons to the acceptor MO molecules. The –N=N– bonds broke down to –N–N– bonds, which decolorized the MO solution [50].

Further, we studied the influence of Cu@Alg/Co–CeO_2 amount on MO catalytic reduction with the aid of $NaBH_4$, and therefore, the effect of Cu@Alg/Co–CeO_2 amount on the catalytic reduction of MO was assessed (Figure 5). Two, four, and six beads of Cu@Alg/Co–CeO_2 were added individually to the MO solutions having the same volume (2.5 mL) and concentration (0.07 mM) of MO, as well as volume (0.25 mL) and concentration (0.1 M) of $NaBH_4$. Figure 5d demonstrates the % reduction vs. time plot for the present study. Initially, various numbers of Cu@Alg/Co–CeO_2 beads, i.e., two, four, and six beads, were utilized and tested as catalysts for MO reduction using $NaBH_4$. The recorded absorbance by UV–vis evidently showed a continuous decrease in absorbance with the passage of time, and this decrease in absorbance was much faster in the case of six beads as compared to four beads and two beads, i.e., increasing the catalyst amount increased the rate of reduction. Different amounts of Cu@Alg/Co–CeO_2 decolorized MO solutions in 9.0, 9.0, and 32.0 min, respectively. Hence, it was discovered that a high amount of Cu@Alg/Co–CeO_2 helps to reduce MO faster as compared to a smaller amount, and thus six beads of Cu@Alg/Co–CeO_2 were more effective than four and two beads. The examined solutions containing 0.07 mM MO were completely decolorized within 9.0 min using six beads of Cu@Alg/Co–CeO_2. However, decreasing the Cu@Alg/Co–CeO_2 amount to two beads increased the time required for terminating the reduction to 32.0 min to completely reduce the MO. Figure 5d shows that increasing the Cu@Alg/Co–CeO_2 amount from two beads to six beads caused a decrease in time for complete reduction of MO. The results indicated that a high amount of Cu@Alg/Co–CeO_2 can eliminate MO from water more

easily, owing to the exposure of more sites for the reduction of MO, and thus can quickly reduce MO as compared to a low quantity of Cu@Alg/Co–CeO_2, which takes a long time to complete the reaction. Thus, increasing the beads' number accelerates the reaction and reduces the time for reaction completion. The reason for the acceleration of the reduction reaction is that a high amount of Cu@Alg/Co–CeO_2 beads offers a large surface area for the adsorption of reactants and desorption of products.

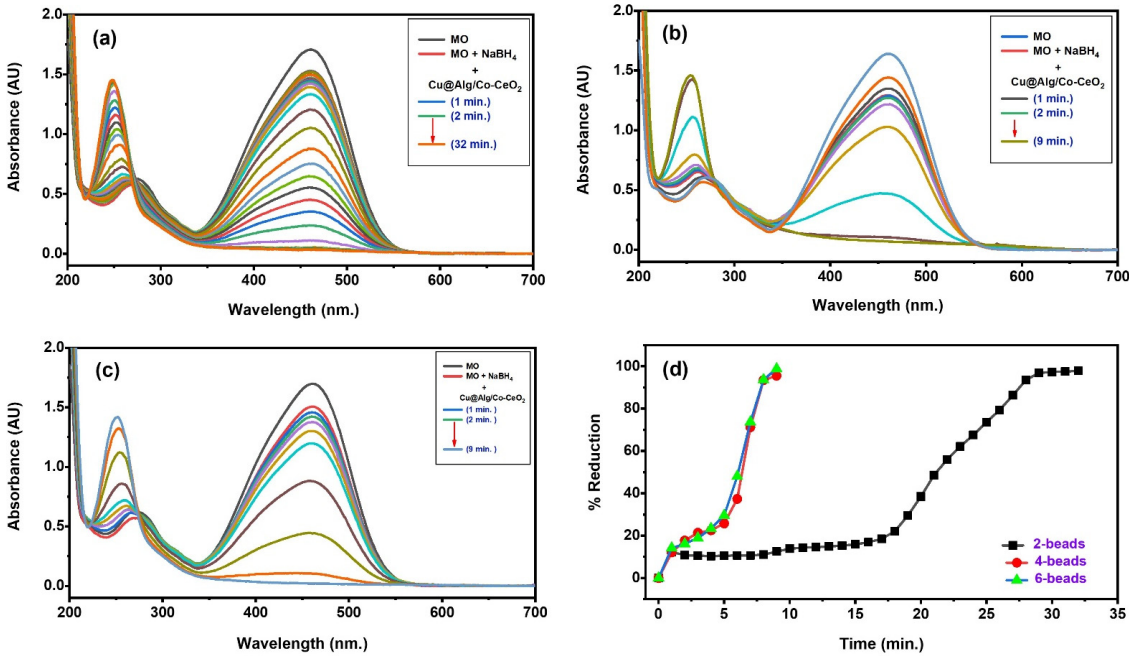

Figure 5. UV–vis absorption spectra for the reduction of MO (0.07 mM) using 0.25 mL $NaBH_4$ (0.1 M) and (**a**) 2 beads, (**b**) 4 beads, and (**c**) 6 beads of Cu@Alg/Co–CeO_2 catalyst. (**d**) % Reduction of MO as a function of time.

The influence of $NaBH_4$ amount (0.25 mL and 0.5 mL) was studied on the catalytic reduction of MO using six beads of Cu@Alg/Co–CeO_2. As displayed in Figure 6, the decrease in $NaBH_4$ concentration led to more time for completing the reduction process. This is ascribed to the significant role of the reducing agent and catalyst since treatment of pollutants with $NaBH_4$ alone cannot reduce time without a catalyst. MO was reduced up to more than 97% with $NaBH_4$ (0.25 mL and 0.5 mL of 0.1 M) in 9.0 min and 4.0 min, respectively. Thus, we can conclude that the reduction rate becomes speedier with increasing the amount of $NaBH_4$.

The reusability of Cu@Alg/Co–CeO_2 was assessed for MO reduction. Stability and recyclability were clearly observed several times with a slight loss in catalytic activity. Figure 7 represents the time taken for MO reduction in each cycle using the same Cu@Alg/Co–CeO_2 beads, which means sensible recyclability of Cu@Alg/Co–CeO_2. The recyclability results signify the stability and recyclability of Cu@Alg/Co–CeO_2, which reduced MO in 12 min until the 6th cycle. The results exhibited that the required time for completing the reaction increased within six consecutive reusability times. These data indicate that Cu@Alg/Co–CeO_2 has plausible reusability and stability. Figure 7g reveals that Cu@Alg/Co–CeO_2 reduced MO in 12 min even until the 6th cycle, signifying the efficient activity of Cu@Alg/Co–CeO_2 toward MO reduction despite the slight loss in activity after each cycle, which is commonly observed in the majority of catalytic reactions, even with highly stable catalysts. The decrease in activity of Cu@Alg/Co–CeO_2 could either be due to the oxidation or release of Cu nanoparticles from the support. Thus, the designed beads are efficient, stable, and recyclable, offering easy recovery from the reaction media. Thus, nanocomposition contributed a significant role in enhancing catalytic characteristics [42,51].

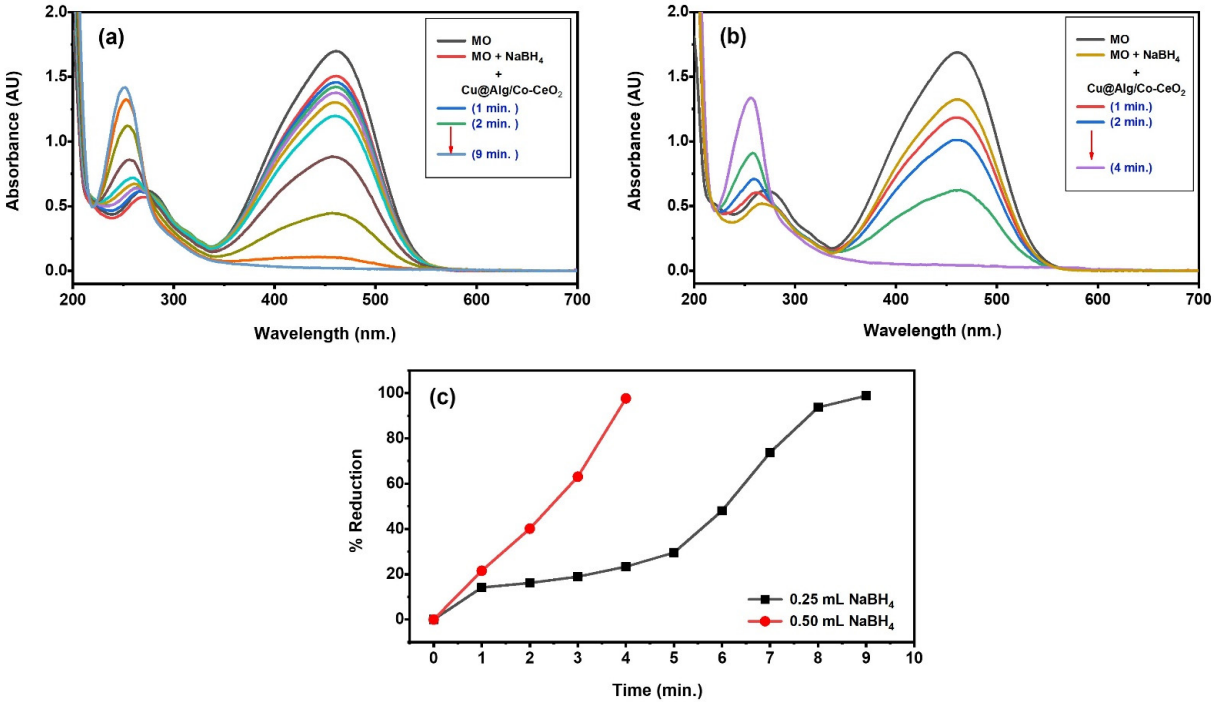

Figure 6. UV–vis absorption spectra for the reduction of MO (0.07 mM) using (**a**) 0.25 mL, (**b**) 0.5 mL $NaBH_4$ (0.1 M), and Cu@Alg/Co–CeO_2 catalyst (6 beads). (**c**) % Reduction of MO as a function of time.

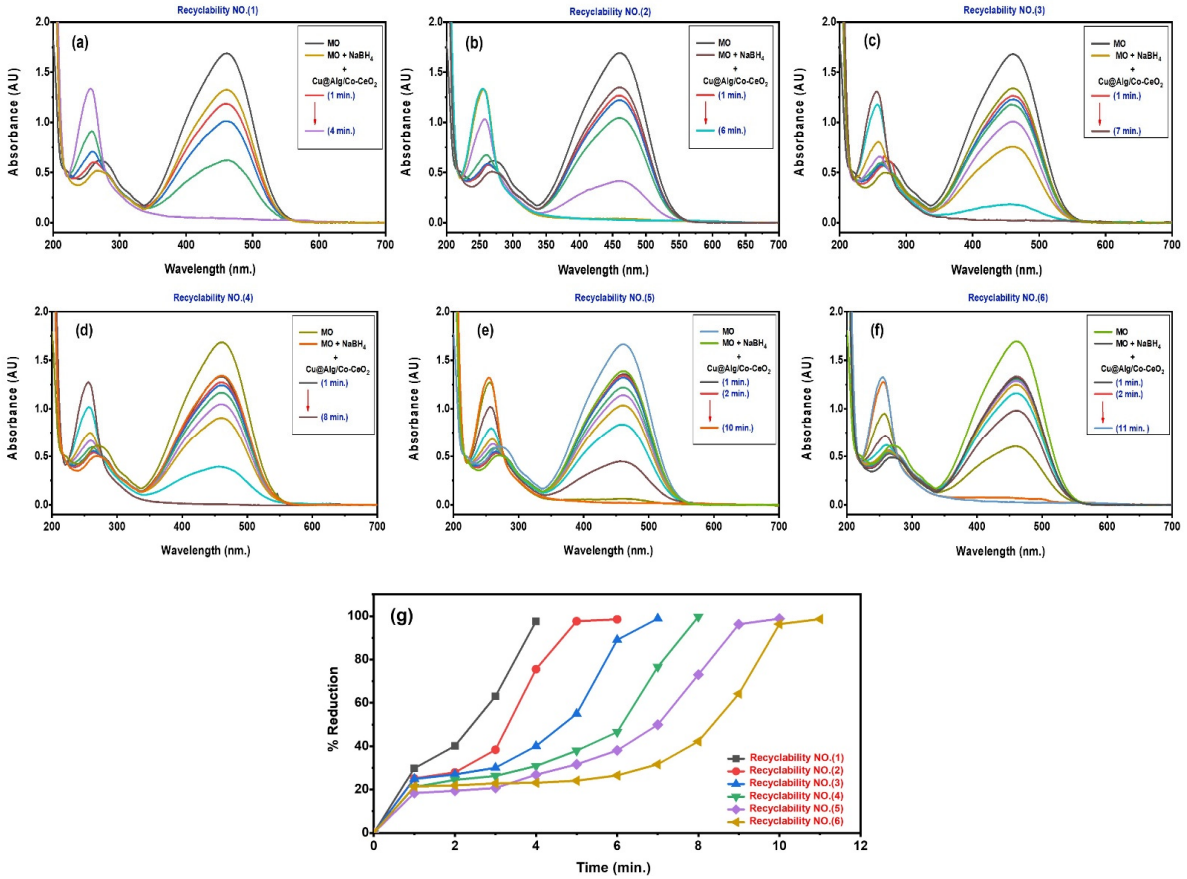

Figure 7. UV–vis absorption spectra for the reduction of MO (0.07 mM) using 0.5 mL $NaBH_4$ (0.1 M) and Cu@Alg/Co–CeO_2 catalyst (6 beads): (**a**) 1st cycle, (**b**) 2nd cycle, (**c**) 3rd cycle, (**d**) 4th cycle, (**e**) 5th cycle, and (**f**) 6th cycle. (**g**) % Reduction of MO as a function of time.

The possible mechanism for MO reduction in the presence of Cu@Alg/Co–CeO_2 is shown in Scheme 1. Initially, BH_4^- attacks MO molecules adsorbed on Cu@Alg/Co–CeO_2, where transfer of electron and hydrogen takes place from BH_4^- to MO. These electrons, which are carried via Cu@Alg/Co–CeO_2, cause activation and breakage of azo bonds in MO [25] by converting –N=N– to –HN–NH– and then break down –HN–NH– to amines. So, decolorized MO solution indicates catalytic reduction of MO. Thus, Cu@Alg/Co–CeO_2 transfers electrons from BH_4^- (donor) to MO (acceptor) and thus causes acceleration of the MO reduction process.

3.2.2. Photocatalytic Degradation

In this study, the removal of dyes was carried out under solar light using Cu@Alg/Co–CeO_2 as a photocatalyst instead of reducing agents. The effectiveness of Cu@Alg/Co–CeO_2 beads was tested for the photocatalytic degradation of a series of pollutants such as MO (0.07 mM), ArO (0.07 mM), CR (0.07 mM), and MB (0.07 mM) under solar light. Catalytic degradation was performed using Cu@Alg/Co–CeO_2 under solar light irridiation (Figure 8a–d). Similar experimental conditions were applied for all contaminants. The wavelengths were MO, 460 nm; ArO, 485 nm; CR, 495 nm; and MB, 659 nm. After the addition of Cu@Alg/Co–CeO_2, a decrease in peak intensity was noticed with time, indicating the photodegradation of dyes by Cu@Alg/Co–CeO_2 under solar light. Figure 8 displays that the absorbance band of dyes decreased steadily while completing the degradation reaction. Figure 8 indicates that degradation of ArO is faster among all studied dyes, which indicates that Cu@Alg/Co–CeO_2 degraded ArO more efficiently. Cu@Alg/Co–CeO_2 degraded ArO in 5 h, while Cu@Alg/Co–CeO_2 did not degrade other dyes even in 5 h.

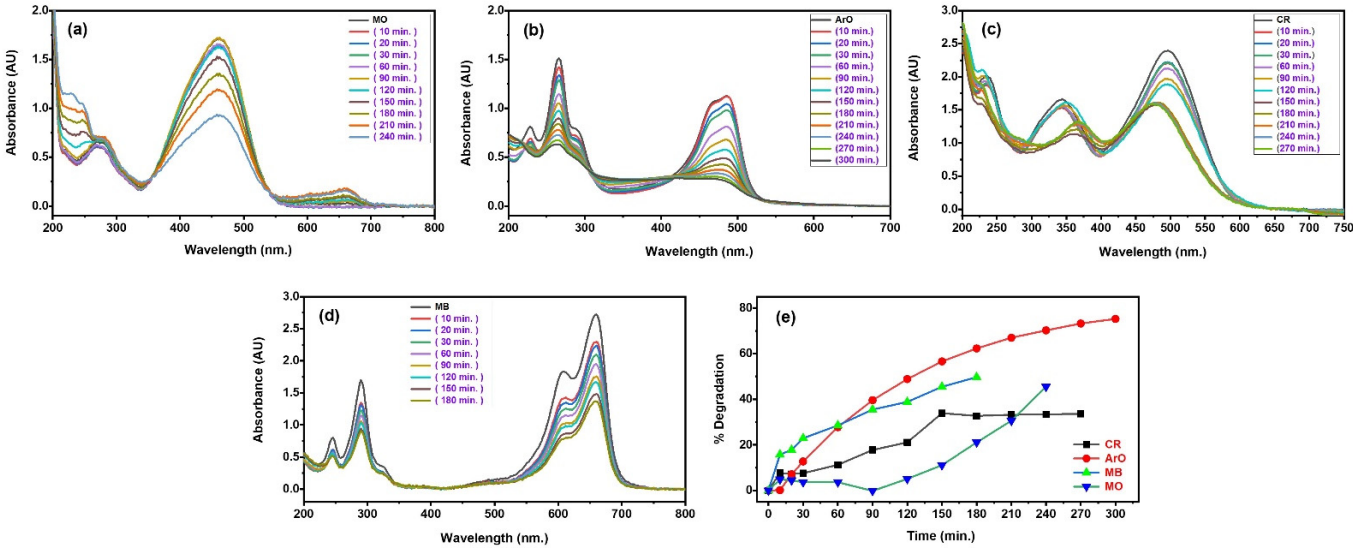

Figure 8. UV–vis absorption spectra for the photodegradation of (**a**) MO (0.07 mM), (**b**) ArO (0.07 mM), (**c**) CR (0.07 mM), and (**d**) MB (0.07 mM) under solar light using Cu@Alg/Co–CeO_2 catalyst (4 beads). (**e**) % Degradation of ArO as a function of time.

The % degradation was calculated by Equation (1), and the % degradation of different dyes is shown in Figure 8e, where degradation of ArO reached about 75.26% in 5 h, while low photodegradation was achieved for other dyes. The obtained data of Cu@Alg/Co–CeO_2 activity in degrading dyes under solar light are as follows: MO, 45.54% at 240 min; ArO, 75.26% at 300 min; CR, 33.65% at 270 min; and MB, 49.70% at 180 min (Figure 8e). Cu@Alg/Co–CeO_2 demonstrated superior catalytic activity toward ArO under sunlight. Thus, Cu@Alg/Co–CeO_2 was more effective and efficient in the reduction of ArO. The fast decrease in absorption suggests that Cu@Alg/Co–CeO_2 beads are effective catalysts for the degradation and mutagenic disruption of ArO, thus boosting photocatalytic activity. This study showed that Cu@Alg/Co–CeO_2 beads are the better catalyst in the photodegradation

of ArO dye. In addition, it was noticed that ArO was photodegraded by around 75% by Cu@Alg/Co–CeO_2 among the tested dyes. This behavior suggests that Cu@Alg/Co–CeO_2 is a perfect choice for ArO degradation. Therefore, ArO was chosen for detailed analysis, where we optimized the catalyst amount and recyclability.

As the catalyst amount plays a significant role in photocatalysis, we studied the degradation of ArO using different catalyst dosages. The effect of catalyst amount on reaction rate was investigated by adding four different amounts (4 beads, 6 beads, 8 beads, and 10 beads) of Cu@Alg/Co–CeO_2 for the degradation of 0.07 mM ArO under solar light conditions (Figure 9). Figure 9e displays % degradation vs. time. It is clear that degradation rate increases with increasing catalyst amount. ArO concentration decreased very fast in the case of 10 beads, and thus the effect of Cu@Alg/Co–CeO_2 quantity led to a positive impact on photodegradation by increasing the total number of active sites. These findings indicate that the photocatalytic reaction is related to the Cu@Alg/Co–CeO_2 quantity, i.e., the photocatalytic degradation increases with an increasing amount of Cu@Alg/Co–CeO_2. A decrease in ArO absorbance was noticed with increasing time, indicating high removal percentage for ArO using 10 beads of Cu@Alg/Co–CeO_2 under solar light, which indicates that Cu@Alg/Co–CeO_2 amount plays an important role in ArO photodegradation. Figure 9 presents that 85% of ArO was degraded in 5 h using 10 beads, while % degradation for ArO was 75.27% (4 beads), 85.71% (6 beads), and 85.71% (8 beads).

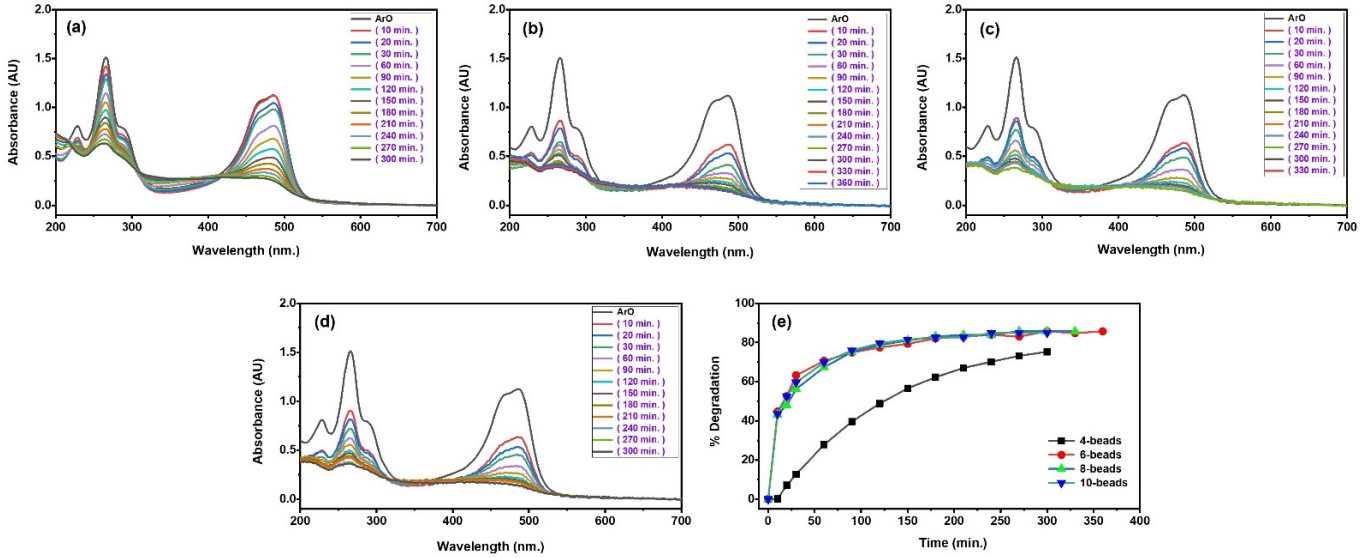

Figure 9. UV–vis absorption spectra for the photodegradation of ArO (0.07 mM) under solar light using (**a**) 4 beads, (**b**) 6 beads, (**c**) 8 beads, and (**d**) 10 beads of Cu@Alg/Co–CeO_2 catalyst. (**e**) % Degradation of ArO as a function of time.

Light plays a significant role in photocatalysis, so we determined the degradation of ArO under sunlight compared with solar light produced by a solar simulator. Figure 10 represents the effect of light, where degradation under the solar simulator light is slightly high as compared to sunlight. Solar produces pure solar light, while sunlight is a mixture of solar and UV light, which might be the reason for slightly lower degradation under sunlight. Figure 10 clearly indicates that the trend of photodegradation is similar; however, 75% of ArO was degraded under sunlight, while 85% of ArO was degraded under solar light using 10 beads.

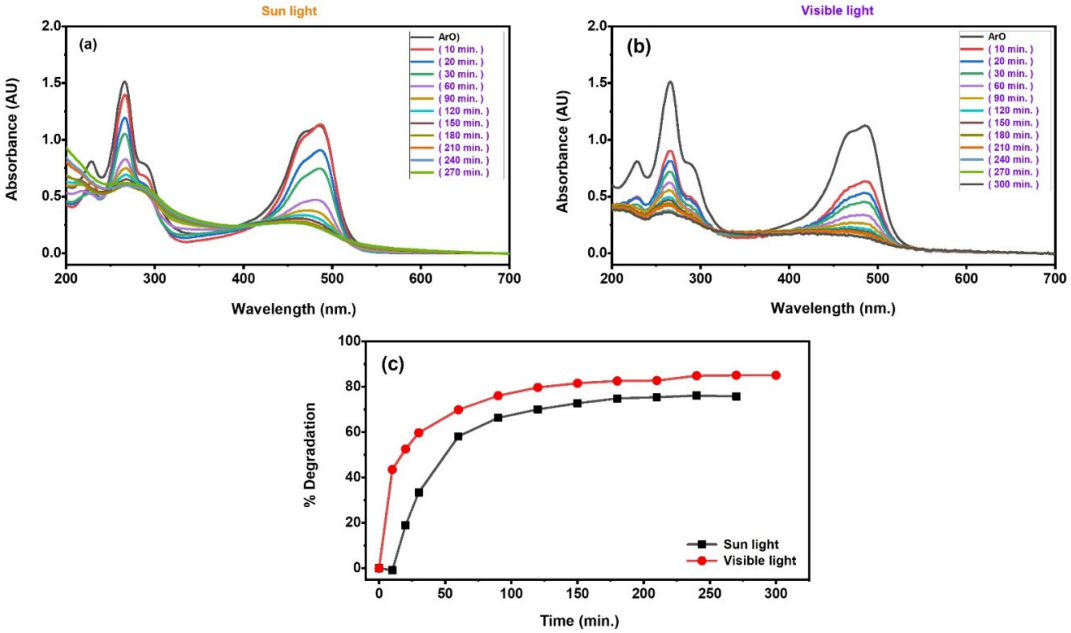

Figure 10. UV–vis absorption spectra for the photodegradation of ArO (0.07 mM) under (**a**) sunlight and (**b**) solar light using Cu@Alg/Co–CeO_2 catalyst (10 beads). (**c**) % Degradation of ArO as a function of time.

Moreover, we studied the recyclability to explore the outstanding characteristics of Cu@Alg/Co–CeO_2 in reusability for several cycles. First, four beads of Cu@Alg/Co–CeO_2 were utilized, separated, washed with distilled water, dried, and reused in another run. Cu@Alg/Co–CeO_2 was reused for four cycles. Figure 11 reveals degradation of ArO in the first cycle (% degradation = 75.27%), second cycle (% degradation = 71.44%), third cycle (% degradation = 70.19%), and fourth cycle (% degradation = 73.39%) at 270 min. It can clearly be observed that % degradation of ArO was nearly constant for all cycles, with a slight decrease in the reaction rate. Comparable results in the literature support the fact of obtaining a slight decrease in reaction rate by employing nanocatalysts in many cycles.

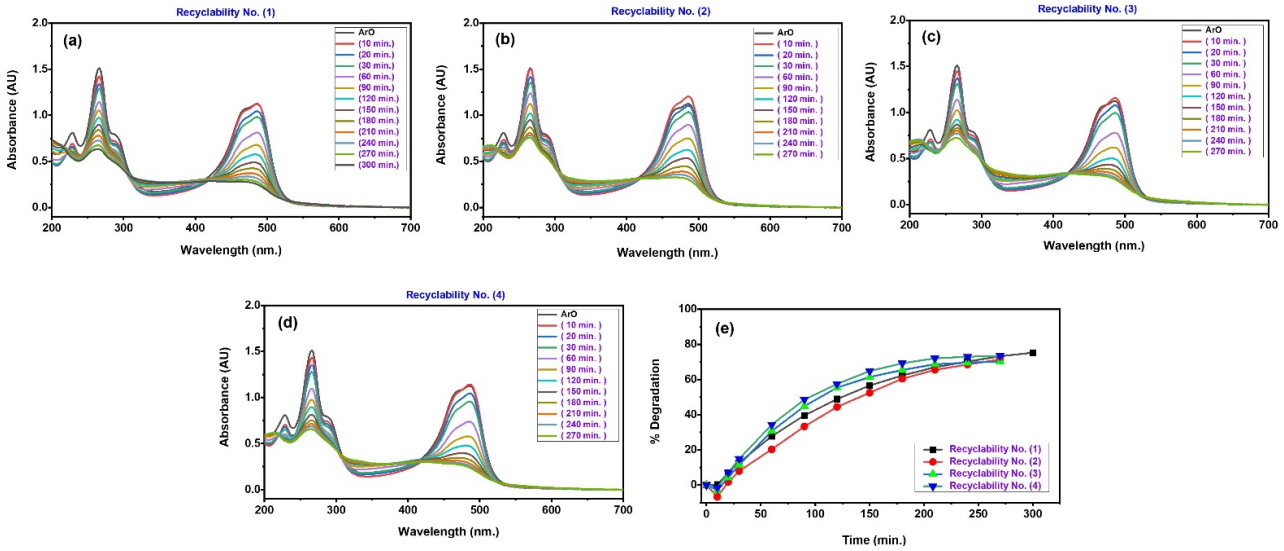

Figure 11. UV–vis absorption spectra for the photodegradation of ArO (0.07 mM) under solar light using Cu@Alg/Co–CeO_2 catalyst (4 beads): (**a**) 1st cycle, (**b**) 2nd cycle, (**c**) 3rd cycle, and (**d**) 4th cycle. (**e**) % Degradation of ArO as a function of time.

The photodegradation mechanism toward organic pollutants is described in Scheme 1. Photon absorption initially occurs due to Cu@Alg/Co–CeO_2, which causes electron excitation from the valence band to the conduction band and generates a positive hole in the valence band:

$$Cu@Alg/Co - CeO_2 + h\nu \rightarrow e^-_{CB} + h^+_{VB}$$

The excited electron in the conduction band ionizes the oxygen that is physically adsorbed on the surface of Cu@Alg/Co–CeO_2.

$$(O_2)_{ads} + e^-_{CB} \rightarrow O_2^{\bullet -}$$

The positive holes convert the hydroxyl group (OH^-) to $OH^\bullet$ and $O_2^{-\bullet}$ to $HO_2^\bullet$.

$$(H_2O \leftrightarrow OH^- + H^+) + h^+_{VB} \rightarrow OH^\bullet + H^+$$

$$H^+ + O_2^{-\bullet} \rightarrow HO_2^\bullet$$

Moreover, $HO_2^\bullet$ is converted into O_2 and H_2O_2.

$$2HO_2^\bullet \rightarrow O_2 + H_2O_2$$

Further, H_2O_2 is decomposed to hydroxyl ion and hydroxyl radical.

$$H_2O_2 \rightarrow OH^- + OH^\bullet$$

Hydroxyl radical and positive holes cause oxidation of ArO.

$$OH^\bullet + R \rightarrow OH + R^\bullet$$

$$R + h^+_{VB} \rightarrow R^{+\bullet} \rightarrow degradation\ products$$

4. Conclusions

A facile synthesis of Cu@Alg/Co–CeO_2 nanoparticles was performed, followed by an investigation of catalytic reduction and photocatalytic degradation of different dyes and nitrophenols. The results revealed that Cu@Alg/Co–CeO_2 is an efficient catalyst that can effectively reduce and degrade MO and ArO in a short time with the aid of $NaBH_4$ and solar light. Cu@Alg/Co–CeO_2 can be simply eliminated from the reaction matrix, making it a recyclable and reusable catalyst. Cu@Alg/Co–CeO_2 offered superb performance toward the catalytic reduction and photocatalytic degradation of MO and ArO, and thus the designed nanocatalyst possesses exceptional effectiveness for complete removal of MO and ArO, which can be promising for water purification purposes.

Author Contributions: H.A.A.; conceptualization, investigation, formal analysis, analysis of data, writing—original draft, writing—review and editing; A.M.A.: conceptualization, editing, funding acquisition; K.A.A.: writing—review and editing; H.M.M.: writing—review and editing; S.Y.A.: writing—review and editing; S.B.K.: writing—review and editing. All authors have read and agreed to the published version of the manuscript.

Funding: Ministry of Education in Saudi Arabia and King Abdulaziz University, DSR, Jeddah, Saudi Arabia.

Institutional Review Board Statement: Not applicable.

Informed Consent Statement: Not applicable.

Data Availability Statement: Not applicable.

Acknowledgments: The authors extend their appreciation to the Deputyship for Research & Innovation, Ministry of Education in Saudi Arabia for funding this research work through the project number (IFPNC-006-130-2020) and King Abdulaziz University, DSR, Jeddah, Saudi Arabia.

Conflicts of Interest: The authors declare no conflict of interest.

References

1. Wang, Y.; Sun, H.; Ang, H.M.; Tadé, M.O.; Wang, S. 3D-hierarchically structured MnO_2 for catalytic oxidation of phenol solutions by activation of peroxymonosulfate: Structure dependence and mechanism. *Appl. Catal. B Environ.* **2015**, *164*, 159–167. [CrossRef]
2. Wang, L.; Ke, F.; Zhu, J. Metal-organic gel templated synthesis of magnetic porous carbon for highly efficient removal of organic dyes. *Dalton. Trans.* **2016**, *45*, 4541–4547. [CrossRef] [PubMed]
3. Dong, F.P.; Guo, W.P.; Parka, S.S.; Ha, C.S. Uniform and monodisperse polysilsesquioxane hollow spheres: Synthesis from aqueous solution and use in pollutant removal. *J. Mater. Chem.* **2011**, *21*, 10744–10749. [CrossRef]
4. Luo, M.X.; Lv, L.P.; Deng, G.W.; Yao, W.; Ruan, Y.; Li, X.; Xu, A. The mechanism of bound hydroxyl radical formation and degradation pathway of Acid Orange II in Fenton-like Co^{2+}-HCO_3-system. *Appl. Catal. B Environ.* **2014**, *146*, 192–200. [CrossRef]
5. Wang, M.; Liu, X.; Pan, B.; Zhang, S. Photodegradation of Acid Orange 7 in a UV/acetylacetone process. *Chemosphere* **2013**, *93*, 2877–2882. [CrossRef]
6. Salehi, Z.; Rasouli, A.; Doosthosseini, H. p-nitrophenol Degradation Kinetics and Mass Transfer Study by *Ralstonia eutropha* as a Whole Cell Biocatalyst. *Polycycl. Aromat. Compd.* **2019**, *41*, 292–305. [CrossRef]
7. Kulkarni, M.; Chaudhari, A. Biodegradation of *p*-nitrophenol by *P. putida*. *Bioresour. Technol.* **2006**, *97*, 982–988. [CrossRef]
8. Tomei, M.C.; Annesini, M.C. 4-Nitrophenol biodegradation in a sequencing batch reactor operating with aerobic-anoxic cycles. *Environ. Sci. Technol.* **2005**, *39*, 5059–5065. [CrossRef]
9. Tan, C.; Gao, N.; Deng, Y.; An, N.; Deng, J. Heat-activated persulfate oxidation of diuron in water. *Chem. Eng. J.* **2012**, *203*, 294–300. [CrossRef]
10. Oturan, M.A.; Peiroten, J.; Chartrin, P.; Acher, A.J. Complete destruction of p-Nitrophenol in aqueous medium by electro-fenton method. *Environ. Sci. Technol.* **2000**, *34*, 3474–3479. [CrossRef]
11. Kiwi, J.; Pulgarin, C.; Peringer, P. Effect of Fenton and photo-Fenton reactions on the degradation and biodegradability of 2 and 4-nitrophenols in water treatment. *Appl. Catal. B Environ.* **1994**, *3*, 335–350. [CrossRef]
12. Ruan, M.; Song, P.; Liu, J.; Li, E.; Xu, W. Highly Efficient Regeneration of Deactivated Au/C Catalyst for 4-Nitrophenol Reduction. *J. Phys. Chem. C* **2017**, *121*, 25882–25887. [CrossRef]
13. Min, J.; Xu, L.; Fang, S.; Chen, W.; Hu, X. Molecular and biochemical characterization of 2-chloro-4-nitrophenol degradation via the 1,2,4-benzenetriol pathway in a Gram-negative bacterium. *Appl. Microbiol. Biotechnol.* **2019**, *103*, 7741–7750. [CrossRef]
14. Sj, S. The gene cluster for para-nitrophenol catabolism is responsible for 2-chloro-4-nitrophenol degradation in Burkholderia sp. Strain SJ98. *Appl. Environ. Microbiol.* **2014**, *80*, 6212–6222.
15. Mahdi-Ahmed, M.; Chiron, S. Ciprofloxacin oxidation by UV-C activated peroxymonosulfate in wastewater. *J. Hazard. Mater.* **2014**, *265*, 41–46. [CrossRef]
16. Khan, S.A.; Khan, S.B.; Asiri, A.M. Toward the design of Zn–Al and Zn–Cr LDH wrapped in activated carbon for the solar assisted de-coloration of organic dyes. *RSC Adv.* **2016**, *6*, 83196–83208. [CrossRef]
17. Khan, S.A.; Khan, S.B.; Asiri, A.M. Layered double hydroxide of Cd-Al/C for the mineralization and de-coloration of dyes in solar and visible light exposure. *Sci. Rep.* **2016**, *6*, 35107. [CrossRef] [PubMed]
18. Wang, C.; Salmon, L.; Li, Q.; Igartua, M.E.; Moya, S.; Ciganda, R.; Ruiz, J.; Astruc, D. From Mono to Tris-1,2,3-triazole-Stabilized Gold Nanoparticles and Their Compared Catalytic Efficiency in 4-Nitrophenol Reduction. *Inorg. Chem.* **2016**, *55*, 6776–6780. [CrossRef]
19. Kamal, T.; Ahmad, I.; Khan, S.B.; Asiri, A.M. Bacterial cellulose as support for biopolymer stabilized catalytic cobalt nanoparticles. *Int. J. Biol. Macromol.* **2019**, *135*, 1162–1170. [CrossRef]
20. Ismail, M.; Khan, M.; Akhtar, K.; Khan, M.A.; Asiri, A.M.; Khan, S.B. Biosynthesis of Silver Nanoparticles: A Colorimetric Optical Sensor for Detection of Hexavalent Chromium and Ammonia in Aqueous Solution. *Phys. E Low-Dimens. Syst. Nanostructures* **2018**, *103*, 367–376. [CrossRef]
21. Gupta, N.; Singh, H.P.; Sharma, R.K. Metal nanoparticles with high catalytic activity in degradation of methyl orange: An electron relay effect. *J. Mol. Catal. A Chem.* **2011**, *335*, 248. [CrossRef]
22. Khan, M.M.; Lee, J.; Cho, M.H. Au@TiO_2 nanocomposites for the catalytic degradation of methyl orange and methylene blue: An electron relay effect. *J. Ind. Eng. Chem.* **2014**, *20*, 1584. [CrossRef]
23. Khan, S.B.; Ahmad, S.; Kamal, T.; Asiri, A.M.; Bakhsh, E.M. Metal nanoparticles decorated sodium alginate carbon nitride composite beads as effective catalyst for the reduction of organic pollutants. *Int. J. Biol. Macromol.* **2020**, *164*, 1087–1098. [CrossRef] [PubMed]
24. Bastus, N.G.; Merkoci, F.; Piella, J.; Puntes, V. Synthesis of Highly Monodisperse Citrate-Stabilized Silver Nanoparticles of up to 200 nm: Kinetic Control and Catalytic Properties. *Chem. Mater.* **2014**, *26*, 2836. [CrossRef]
25. Jiang, Z.-J.; Liu, C.-Y.; Sun, L.-W. Catalytic Properties of Silver Nanoparticles Supported on Silica Spheres. *J. Phys Chem. B* **2005**, *109*, 1730. [CrossRef]
26. Daniel, M.C.; Astruc, D. Gold nanoparticles: Assembly, supramolecular chemistry, quantum-size-related properties, and applications toward biology, catalysis, and nanotechnology. *Chem. Rev.* **2004**, *104*, 293. [CrossRef]
27. Azad, U.P.; Ganesan, V.; Pal, M. Catalytic reduction of organic dyes at gold nanoparticles impregnated silica materials: Influence of functional groups and surfactants. *J. Nanopart. Res.* **2011**, *13*, 3951. [CrossRef]
28. Khalid, N.R.; Majid, A.; Tahir, M.B.; Niaz, N.A.; Khalid, S. Carbonaceous-TiO_2 nanomaterials for photocatalytic degradation of pollutants: A review. *Ceram. Int.* **2017**, *43*, 14552–14571. [CrossRef]

29. Han, M.; Zhu, S.; Lu, S.; Song, Y.; Feng, T.; Tao, S.; Liu, J.; Yang, B. Recent progress on the photocatalysis of carbon dots: Classification, mechanism and applications. *Nano Today* **2018**, *19*, 201–218. [CrossRef]
30. Ismail, M.; Gul, S.; Khan, M.; Khan, M.A.; Asiri, A.M.; Khan, S.B. Green synthesis of zerovalent copper nanoparticles for efficient reduction of toxic azo dyes congo red and methyl orange. *Green Processing Synth.* **2019**, *8*, 135–143. [CrossRef]
31. Jang, E.S.; Khan, S.B.; Seo, J.; Nam, Y.H.; Choi, W.J.; Akhtar, K.; Han, H. Synthesis and characterization of novel UV-curable polyurethane–clay nanohybrid: Influence of organically modified layered silicates on the properties of polyurethane. *Prog. Org. Coat.* **2011**, *71*, 36–42. [CrossRef]
32. Lee, Y.; Kim, D.; Seo, J.; Han, H.; Khan, S.B. Preparation and characterization of poly(propylene carbonate)/exfoliated graphite nanocomposite films with improved thermal stability, mechanical properties and barrier properties. *Polym. Int.* **2013**, *62*, 1386–1394. [CrossRef]
33. Khan, S.B.; Rahman, M.M.; Jang, E.S.; Akhtar, K.; Han, H. Special susceptive aqueous ammonia chemi-sensor: Extended applications of novel UV-curable polyurethane-clay nanohybrid. *Talanta* **2011**, *84*, 1005–1010. [CrossRef] [PubMed]
34. Thakur, S.; Sharma, B.; Verma, A.; Chaudhary, J.; Tamulevicius, S.; Thakur, V.K. Recent progress in sodium alginate based sustainable hydrogels for environmental applications. *J. Clean. Prod.* **2018**, *198*, 143–159. [CrossRef]
35. Bakhsh, E.M.; Akhtar, K.; Fagieh, T.M.; Khan, S.B.; Asiri, A.M. Development of alginate@ tin oxide–cobalt oxide nanocomposite based catalyst for the treatment of wastewater. *Int. J. Biol. Macromol.* **2021**, *187*, 386–398. [CrossRef]
36. Zahid, M.; Nadeem, N.; Tahir, N.; Un-Nisa, F.; Majeed, M.I.; Mansha, A.; Naqvi, S.A.R.; Hussain, T. Hybrid nanomaterials for water purification. In *Multifunctional Hybrid Nanomaterials for Sustainable Agri-Food and Ecosystems*; Elsevier: Amsterdam, The Netherlands, 2020; pp. 155–188.
37. Khan, S.B.; Khan, M.S.J.; Kamal, T.; Asiri, A.M.; Bakhsh, E.M. Polymer supported metallic nanoparticles as a solid catalyst for the removal of organic pollutants. *Cellulose* **2020**, *27*, 5907–5921. [CrossRef]
38. Khan, S.B.; Alamry, K.A.; Marwani, H.M.; Asiri, A.M.; Rahman, M.M. Synthesis and environmental applications of cellulose/ZrO_2 nanohybrid as a selective adsorbent for nickel ion. *Compos. Part B Eng.* **2013**, *50*, 253–258. [CrossRef]
39. Rahman, M.M.; Khan, S.B.; Faisal, M.; Rahman, M.M.; Akhtar, K.; Asiri, A.M.; Khan, A.; Alamry, K.A. Effect of particle size on the photocatalytic activity and sensing properties of CeO_2 nanoparticles. *Int. J. Electrochem. Sci.* **2013**, *8*, 7284–7297.
40. Khan, S.B.; Asiri, A.M.; Alamry, K.A.; Khan, A.A.P.; Khan, A.; Abdul Rub, M.; Azum, N. Acetone sensor based on solvothermally prepared ZnO doped with Co_3O_4 nanorods. *Microchim. Acta* **2013**, *180*, 675–685.
41. Khan, S.B.; Rahman, M.M.; Marwani, H.M.; Asiri, A.M.; Alamry, K.A. An assessment of zinc oxide nanosheets as a selective adsorbent for cadmium. *Nanoscale Res. Lett.* **2013**, *8*, 377. [CrossRef]
42. Bakhsh, E.M.; Akhtar, K.; Fagieh, T.M.; Asiri, A.M.; Khan, S.B. Sodium alginate nanocomposite based efficient system for the removal of organic and inorganic pollutants from wastewater. *Int. J. Biol. Macromol.* **2021**, *191*, 243–254. [CrossRef] [PubMed]
43. Nasrullah, A.; Khan, A.S.; Bhat, A.H.; Din, I.U.; Inayat, A.; Muhammad, N.; Bakhsh, E.M.; Khan, S.B. Effect of short time ball milling on physicochemical and adsorption performance of activated carbon prepared from mangosteen peel waste. *Renew. Energy* **2021**, *168*, 723–733. [CrossRef]
44. Cai, Z.; Sun, Y.; Liu, W.; Pen, F.; Sun, P.; Fu, J. An overview of nanomaterials applied for removing dyes from wastewater. *Environ. Sci. Pollut. Res.* **2017**, *24*, 15882–15904. [CrossRef] [PubMed]
45. Khan, S.B.; Karimov, K.S.; Chani, M.T.S.; Asiri, A.M.; Akhtar, K.; Fatima, N. Impedimetric sensing of humidity and temperature using CeO_2–Co_3O_4 nanoparticles in polymer hosts. *Microchim. Acta* **2015**, *182*, 2019–2026. [CrossRef]
46. Bakhsh, E.M.; Khan, S.B.; Marwani, H.M.; Danish, E.Y.; Asiri, A.M. Efficient electrochemical detection and extraction of copper ions using ZnSe–CdSe/SiO_2 core–shell nanomaterial. *J. Ind. Eng. Chem.* **2019**, *73*, 118–127. [CrossRef]
47. Khan, S.A.; Khan, S.B.; Asiri, A.M. Electro-catalyst based on cerium doped cobalt oxide for oxygen evolution reaction in electrochemical water splitting. *J. Mater. Sci. Mater. Electron.* **2016**, *27*, 5294–5302. [CrossRef]
48. Khan, S.B.; Akhtar, K.; Bakhsh, E.M.; Asiri, A.M. Electrochemical detection and catalytic removal of 4-nitrophenol using CeO_2-Cu_2O and CeO_2-Cu_2O/CH nanocomposites. *Appl. Surf. Sci.* **2019**, *492*, 726–735. [CrossRef]
49. Khan, S.A.; Khan, S.B.; Farooq, A.; Asiri, A.M. A facile synthesis of CuAg nanoparticles on highly porous ZnO/carbon black-cellulose acetate sheets for nitroarene and azo dyes reduction/degradation. *Int. J. Biol. Macromol.* **2019**, *130*, 288–299. [CrossRef]
50. Akhtar, K.; Ali, F.; Sohni, S.; Kamal, T.; Asiri, A.M.; Bakhsh, E.M.; Khan, S.B. Lignocellulosic biomass supported metal nanoparticles for the catalytic reduction of organic pollutants. *Environ. Sci. Pollut. Res.* **2020**, *27*, 823–836. [CrossRef]
51. Maslamani, N.; Khan, S.B.; Danish, E.Y.; Bakhsh, E.M.; Zakeeruddin, S.M.; Asiri, A.M. Carboxymethyl cellulose nanocomposite beads as super-efficient catalyst for the reduction of organic and inorganic pollutants. *Int. J. Biol. Macromol.* **2021**, *167*, 101–116. [CrossRef]
52. Danish, M.S.; Estrella, L.L.; Alemaida, I.M.A.; Lisin, A.; Moiseev, N.; Ahmadi, M.; Nazari, M.; Wali, M.; Zaheb, H.; Senjyu, T. Photocatalytic Applications of Metal Oxides for Sustainable Environmental Remediation. *Metals* **2021**, *11*, 80. [CrossRef]
53. Zhang, K.; Suh, J.M.; Choi, J.-W.; Jang, H.W.; Shokouhimehr, M.; Varma, R.S. Recent advances in the nanocatalyst-assisted $NaBH_4$ Reduction of Nitroaromatics in Water. *ACS Omega* **2019**, *4*, 483–495. [CrossRef] [PubMed]
54. Liu, L.; Corma, A. Metal catalysts for heterogeneous catalysis: From single atoms to nanoclusters and nanoparticles. *Chem. Rev.* **2018**, *118*, 4981–5079. [CrossRef] [PubMed]